ORIGINAL PAPER

New insights into the photoassisted anodic reactions of n-type 4H SiC semiconductors

Katharina Mairhofer[1] · Silvia Larisegger[2] · Annette Foelske[3] · Markus Sauer[3] · Gernot Friedbacher[1] · Günter Fafilek[1]

Abstract

This study aims to investigate the photoelectrochemical behavior of the n-type 4H-SiC, focusing on aqueous, hydroxide-based electrolytes. Despite its high stability, this wide-bandgap semiconductor material undergoes electrochemical reactions, such as anodic oxidation or etching, under specific conditions. Since electrons are the majority charge carriers in n-type semiconductors, oxidation processes require above-bandgap illumination. Then, the reaction rate is influenced by the number of electron holes available for an oxidation process and the velocity of the transport of hydroxide ions to/from the surface. The goal is to focus on the essential reaction parameters (i.e., potential and electrolyte concentration) to clarify the reaction mechanism in aqueous (alkaline) electrolytes. Methods with controllable hydrodynamic conditions are required to investigate the transport processes in the electrolyte. Even though the rotating disk electrode (RDE) is a commonly used and powerful method, it is not well suited for our purpose. Photoelectrochemical etching of SiC is extraordinary because it involves both mass transfer phenomena and gas evolution but also needs high-intensity illumination from an appropriate light source. Hence, a new concept for an inverted rotating cell was developed and implemented. This setup was used to study the effect of the mass transport of hydroxide ions on the photoelectrochemical behavior of SiC in each potential region at varying rotation speeds. In order to interpret the experimental findings, a distinct electrical network model was formulated for simulating the results, aiding in unraveling the underlying reaction mechanism. Electrochemical measurements were complemented by surface-sensitive analytical techniques. XPS was the method of choice to investigate the composition of the sample surface before and after etching. SEM and AFM allow the characterization of the surface morphology in the initial stages of etching. The totality of this information provides a complete picture of the complex processes in the vicinity of the semiconductor electrode.

Graphical abstract
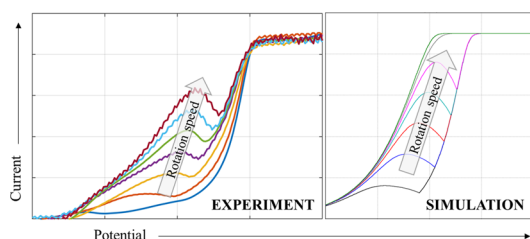
Introduction

The past two decades have experienced a rapid emergence of the silicon carbide (SiC) technology. The main motivation for the introduction of wide-bandgap semiconductors has been to overcome the limitations of silicon, which has

---

Extended author information available on the last page of the article

been the standard in the semiconductor industry for more than 50 years. Among the long list of desirable material properties are high hardness, mechanical stability, thermal conductivity, and resistance against oxidation and corrosion. The ability to operate under severe conditions sets SiC apart from other materials and makes it ideal for devices operating in harsh environments. Due to its outstanding physical, chemical, electrical, and thermal material properties, SiC is attractive for a variety/broad range of industrial applications, such as power devices [1–3], photonic devices [4], micro-electro-mechanical systems (MEMS) [4], and sensors [5], including biosensors [6].

While 3C-SiC is interesting for MEMS applications, power electronics have a strong focus on the 4H material due to the high breakdown electric field and saturation drift velocity [5]. Power electronics have been following the trend towards higher efficiency and power density as well as more integrated systems [3]. The low intrinsic carrier concentration compared to silicon, which is a result of the wider bandgap, enables the operation at higher temperatures. This makes SiC the prime candidate for high voltage, high temperature, and high switching frequency applications [7]. SiC technology continues to mature rapidly, with many power devices now being commercialized (e.g., Schottky diodes, MOSFETs, JFETs, BJTs) [2]. Others, such as SiC IGBTs, are still in their infancy. There, a major interest also lies in the quality and reliability of the SiC/SiO_2 interface [8]. Sophisticated manufacturing processes, such as the emerging silicon carbide on insulator technology (SiCOI), open up new opportunities for the use of SiC in photonic circuits [9].

Since the first commercialization of SiC wafers, the interest in the material has seen an impressive boost. Despite the impeccable development, the high material and manufacturing costs remain the main challenge for the widespread implementation of SiC systems. Besides the higher costs for the base material, the prices also suffer due to the intensive and, to some point, immature production processes of SiC devices. Hence, there is a tremendous demand to reduce costs through the improvement of manufacturing processes.

Etching is an essential method in device fabrication for the systematic removal of material. Both dry and wet etching techniques find specific applications in the semiconductor industries. Dry etching processes, such as ion bombardment or plasma etching, are based on the physical interaction of matter. They are characterized by their low selectivity and high anisotropy. Reactive ion etching (RIE) is currently the most common microstructuring technique [10, 11]. Disadvantageously, the bombardment with ions sometimes leads to severe subsurface damage. Also, in comparison to dry etching processes, wet chemical etching is relatively inexpensive, achieves high etch rates, and requires less complicated equipment [12]. Thus, wet chemical etching is a fast and low-cost alternative to dry etching techniques [11].

However, no chemical is known to cause damage to SiC at room temperature without further external stimulation. This chemical stability poses a challenge for manufacturing processes. As the crystal structure is impervious to the diffusion of atoms, chemical etchants are not able to attack the backbones of the material [11]. Consequently, SiC is unaffected by chemical etching at room temperature. Chemical etching only becomes feasible in molten salts at temperatures > 400 °C [12]. In contrast, photoassisted electrochemical etching is possible under moderate conditions and with relatively simple equipment.

Early work concerning the photoelectrochemistry of SiC goes back to 1984 from Morisaki et al. [13], who investigated the properties of n-type single crystals for their potential use in photoelectrochemical water splitting. Instead of water oxidation, they found the formation of a SiO_x layer (i.e., photocorrosion) of the material. For a long time, the investigation of (photoassisted) anodic etching of silicon carbide was determined by the availability—or rather the lack—of high-quality crystalline wafers. The first studies were conducted on cubic (β-) SiC. Shor and Osgood [14, 15] published a method for etching n-type SiC using light-generated carriers in diluted HF. Trenches were formed by direct writing using green-light and UV lasers. For etching broad areas, the authors used UV lamps combined with metal masks and standard lithography technology while applying a constant anodic voltage. With this, a new technique for microstructural patterning of SiC was introduced. Little later, Shor and coworkers continued their series of work with reports on the photoassisted anodic etching of α-SiC [10, 16], performed under similar experimental conditions.

Most of the literature up to this day is focused on HF or HF-based solutions as electrolytes. The first description of etching 6H-SiC in KOH solutions was given in 2003 by Kato et al. [17]. They varied etching parameters, including electrolyte concentration, temperature, UV light illumination, and current density. A thorough investigation of the (photo) electrochemistry of both p- and n-type 4H/6H-SiC wafer materials was done by Van Dorp et al. in alkaline solutions [18, 19] and in HF [20, 21].

The rapid and cost-saving fabrication of micro-electromechanical systems (MEMS) is one of the main fields of interest for wet chemical etching of silicon carbide. Zhao et al. employed dopant-selective etching to fabricate microstructures in single-crystal 4H-SiC. They achieved the fabrication of cantilevers and suspended bridges by underetching p-SiC structures, using a KOH solution as an electrolyte. This micromachining process allowed well-controllable, rapid, and simple structuring of wafers and the integration of electronic devices and circuits on the same chip [22]. In the search for novel MEMS device concepts, Leitgeb et al. [23, 24] performed metal- assisted photochemical etching (MAPCE) prior to the porosification of 4H-SiC in HF to

create uniformly distributed pore initiation sites. Recently (i.e., in 2023), a work for microstructuring SiC with nanometer-scale precision for use in MEMS and quantum devices was published. Whiteley et al. [25] proposed a method to prepare single-crystalline 4H-SiC on insulator using photoelectrochemical etching.

Despite the wide range of publications available in the literature, the details of the reaction mechanism are still not fully understood. While previous works focus primarily on phenomenological studies, this work aims at gaining a deep understanding of the electrode processes playing into the oxidation and dissolution behavior of 4H-SiC in alkaline solutions. For that purpose, a completely new setup, custom-designed for the investigation of photoelectrochemical processes involving gaseous reaction products, was employed. Systematic analytical measurements helped to identify and distinguish different reaction regimes. With this knowledge, new and advanced processes to structure SiC wafers in a more inexpensive and less time-consuming manner can be developed.
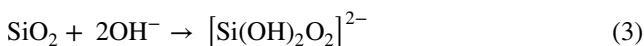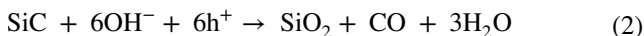
Results and discussion

Measurements in the static cell

The (photo)electrochemistry of SiC in alkaline solutions was extensively studied by Van Dorp et al. [18]. For the photoassisted anodic dissolution of SiC in hydroxide solutions, the following reaction was proposed:

$$SiC + 8OH^- + 6h^+ \rightarrow \left[Si(OH)_2O_2\right]^{2-} + CO + 3H_2O \tag{1}$$
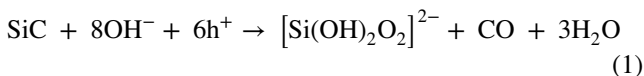
This reaction again comprises two subsequent steps:

$$SiC + 6OH^- + 6h^+ \rightarrow SiO_2 + CO + 3H_2O \tag{2}$$

$$SiO_2 + 2OH^- \rightarrow \left[Si(OH)_2O_2\right]^{2-} \tag{3}$$

Whether the material is oxidized Eq. (2) or dissolved Eq. (2) + Eq. (3) depends of the relative rate constants of the two partials reactions. With no hydroxide ions available at the surface, water molecules may act as oxygen source for the oxidation:

$$SiC + 3H_2O + 6h^+ \rightarrow SiO_2 + CO + 6H^+ \tag{4}$$
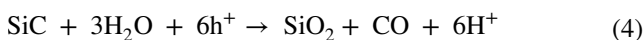
In an alkaline solution, hydronium ions migrate away from the surface and react to water in the bulk solution:

$$H^+ + OH^- \rightarrow H_2O \tag{5}$$

In their studies, Van Dorp et al. performed cyclic voltammograms in a concentration range from 0.05 to 0.5 M KOH.

They found that for low light intensities, the current was limited by the photogenerated hole flux. For high light intensities, the curves showed a distinct peak with a maximum at around $0.55\ V_{SCE}$. Afterward, the current quickly decreased to a constant value, which is typical for the passivation of a semiconductor [19]. The reaction equations proposed for aqueous hydroxide solutions in Eqs. (1) and (4) assume that silicon would most likely form a Si(IV) product and significantly more CO than CO_2 is formed [18]. In the present work, however, a more general approach, which is valid over a wider potential and concentration range, is adopted. Thus, the formation of both CO and CO_2 as reaction products needs to be considered. The further oxidation of CO to CO_2 with either OH^- or water molecules is described by Eqs. (6) and (7), respectively. These Faradaic reactions become more favorable at more positive potentials.

$$CO + 2OH^- + 2h^+ \rightarrow CO_2 + H_2O \tag{6}$$

$$CO + H_2O + 2h^+ \rightarrow CO_2 + 2H^+ \tag{7}$$
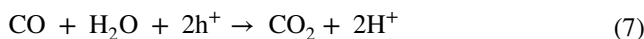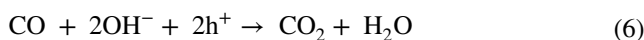
While silicon is oxidized to solid SiO_2, carbon is removed either as gaseous CO and CO_2. In the bulk electrolyte, CO_2 may react soluble HCO_3^-/CO_3^{2-} depending on the pH of the solution.

$$CO_2 + 2OH^- \rightarrow CO_3^{2-} + H_2O \tag{8}$$
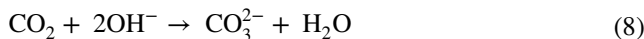
In the present work, we focused on the low concentration regime (below 0.1 M), where mass transport phenomena play an increased role in the overall reaction. Cyclic voltammograms were measured under constant UV irradiation ($\lambda = 365$ nm) for electrolytes containing 1, 2, 5, 10, and 20 mM KOH (Fig. 1). KNO_3 was added to all solutions as a
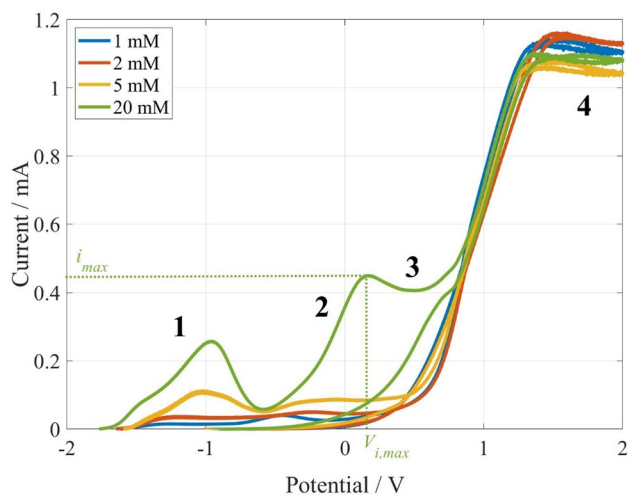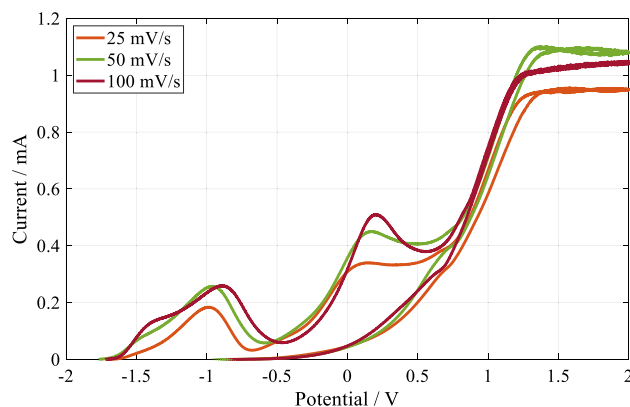
Fig. 1 CVs measured in the static cell at a scan rate of 50 mV s^{-1} for concentrations from 1 to 20 mM KOH. 1st scan is shown

supporting electrolyte to keep a constant concentration of K^+ at 0.1 M. For all solutions prepared this way, conductivities were comparable with about 12.3 ± 0.7 ms cm^{-1}. One scan was performed for each concentration with a scan rate of 50 mV s^{-1}. Measurements were conducted starting from the OCP (approx. -1.5 V) to anodic potentials. Four potential regions were identified and labeled with **1**, **2**, **3**, and **4**. The first oxidation peak (**1**) below -0.5 V, labeled as "pre-peak", only appears in the first cycle of each measurement, and its appearance is easily prevented by shortly polarizing the sample at a potential ≥ -0.75 V. Hence, it must result from the initial surface condition of the silicon carbide wafer. However, the origins of this "pre-peak" are not the focus of this paper. In regions **2** and **3**, the curves demonstrate a clear concentration dependence. The emergence of this peak is the result of a complex reaction mechanism, which will be elucidated using a network model in a later section (see Fig. 11). The maximum peak current increases with hydroxide concentration. Also, the corresponding potential ($V_{i,max}$) is shifted towards more positive values. Comparing region **2** for 1 mM and 20 mM reveals that the slope at the onset of the curve becomes more and more damped with the decrease in hydroxide concentration even though the conductivity remains the same when KNO$_3$ is used as a supporting electrolyte. The shape of the peak is typical for a continuous depletion of a reactant, which is likely to be OH$^-$. Thus, the different curve shapes in regions **2** and **3** hint at a lower rate of oxide formation (and dissolution) due to the slow diffusion of OH$^-$. The material is etched as long as the oxidation is the slowest step, i.e., in 0.02 M KOH below the peak potential. It is most likely that holes generated close to the interface participate in the reaction. At even more positive potentials than 0.75 V (**4**), dominated by the reaction in Eq. (4), all curves show the same behavior independent of the amount of OH$^-$. Oxidation currents rise once more until a plateau is reached. The photoinduced current does not depend on the hydroxide concentration since water molecules act as the oxidizing species. Experiments with varying light intensities suggest that the current in this potential region is limited by the amount of UV light, i.e., the photons available for the generation of electron–hole pairs. In this potential range, the sample is oxidized for all concentrations lower than 0.05 M KOH. This is in good agreement with the findings of Morisaki et al. [13], who described a shift in onset potential between pH 11 and 12 in their cyclic voltammograms, which they also explained by the oxygen source switching from H$_2$O to OH$^-$ beyond a specific hydroxide concentration. With it comes the transition from the photoassisted anodic oxidation to the photoassisted anodic etching of SiC.

Theoretically, the onset potential (V_{on}) of the anodic reaction should be close to the flat-band potential (V_{FB}) of the semiconductor material. For potentials more positive than the flat-band potential, holes move toward the semiconductor-electrolyte interface. However, the electric field is not strong enough to effectively separate the charge carriers for small anodic potentials. Recombination of electrons and holes prevails. This results in a significant overpotential, as observed in Fig. 1. Redox reactions in the solution (e.g., O$_2$ evolution) may compete with the anodic dissolution of the semiconductor material. In general, it is difficult to predict whether a semiconductor mediates a redox reaction or undergoes photocorrosion [26]. The evolution of O$_2$ has never been confirmed for SiC [27].

Instead, the electrode material is altered as soon as the applied potential passes V_{on}. Thus, to investigate the reaction mechanism, experimental conditions need to be chosen so that the electrode surface is not too severely modified in comparison to the initial state. If feasible, the upper vertex potential should not extensively exceed V_{on} and only the first scan should be evaluated for interpretation since applying an anodic bias even for only a few seconds is enough to alter the electrode irreversibly [28]. The scan rate determines the time scale of an experiment. For high upper vertex potentials and slow scan rates, the surface condition between the first and second scan, or even the beginning and the end of a scan, may change significantly. Figure 2 illustrates CVs measured in 20 mM KOH at three different scan rates. For 100, 50, and 25 mV s^{-1}, one scan takes 80, 160, and 320 s, respectively. For reversible, diffusion-controlled reactions, the peak current scales with $v^{1/2}$ [29]. Even though the reactions investigated here do not fulfill the first requirement, it makes sense that the concentration-dependent peaks, i.e., **1** and **2** in Fig. 1, show some dependence on the scan rate. The more pronounced peak structure in potential regions **2** and **3** results from the abrupt depletion of hydroxide ions that occurs when the potential is increased quickly. The transition from a pronounced peak to a plateau with a decreasing scan rate once again underlines the diffusion limitation of

**Fig. 2** CVs measured in the static cell at different scan rates in 20 mM KOH + 80 mM KNO$_3$. 1st scan is shown

this regime. In the photolimited regime (**4**), no dependence on the scan rate is expected. The deviations for 100, 50, and 25 mV s^{-1} are not significant compared to the deviations in light intensity stemming from the experimental setup.

To further distinguish the regimes, transient measurements were carried out for 5 min at a constant light intensity for five different electrolyte concentrations from 1 to 20 mM and three potentials (0, 0.5, 1 V). Figure 3 illustrates the first two minutes of the *I–t* plots for 0 V. Depending on the concentration, this potential is either lower or higher than $V_{i,max}$. At first glance, the shape of the *I–t* curves is relatively similar for all concentrations. An exception is seen for the concentration 5 mM, where it takes longer until the steady state is reached with a short plateau of about 10 s. This behavior is typical if the chosen potential falls close to the peak potential $V_{i,max}$ displayed in Fig. 1. The current drops rapidly during the first few seconds and approaches a constant value afterward. At the beginning of the experiment, a large number of hydroxide ions are available for the oxidation reaction. As they are used up in the reaction, more hydroxide ions need to diffuse to the electrode surface from the bulk electrolyte. The buildup of this diffusion layer results in a decrease in current with $i \sim t^{-1/2}$ before a steady state is reached. The diffusion-limited current i_d as a function of time is given by the Cotrell equation Eq. (9).

$$i_d(t) = z \cdot F \cdot A \cdot (c_0 - c_S) \cdot \sqrt{(D/\pi t)} \qquad (9)$$

In Eq. (9), z is the number of charges involved in the electrode reaction, *F* is the Faraday constant, *D* is the diffusion coefficient and *A* is the electrode area. c_0 and c_S represent the bulk and surface concentration, respectively.

Despite the unstirred solution, the current in Fig. 3 does not further decrease but remains (approximately) constant (as usually observed for stirred solutions). Natural convection through density and temperature gradients, as well as
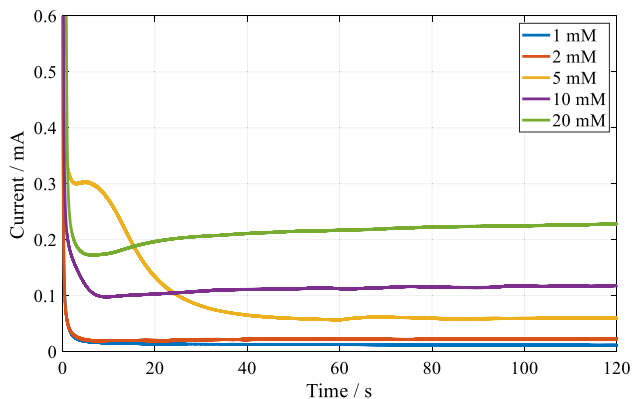

Fig. 3 Transient measurements at 0 V and for different concentrations

gas bubble stirring, are probably responsible. For each but the lowest concentration, the photocurrent is even slightly higher after 120 s than after 60 s. At a concentration of 1 mM, the sample is oxidized; at higher concentrations, SiC is (at least partially) dissolved. This can lead to roughening/surface enlargement, which could explain the increase in current.

Alternating XPS measurements with sputter steps were performed to verify if and to what extent the surface was oxidized. Six samples (the highest and lowest concentration at each potential after 5 min) were analyzed with XPS. The transition showing the transition from the surface to the bulk are displayed in Fig. 4 for two of these samples. The SiC peak is still dominant for a concentration of 20 mM at 0 V (Fig. 4a). Peaks broaden by a factor of about 1.5 as a consequence of Ar$^+$ sputtering from a full width of half maximum (FWHM) of 0.8–0.9 to 1.3–1.4 eV. Residual SiO$_2$ was detected on the surface but was completely removed after sputtering the surface for 60 s (approx. 2 nm). Afterward, only the SiC signal remained. When SiC is etched, the chemistry of the samples remains unchanged, and XPS spectra resemble those of untreated SiC wafers. Therefore, a dissolution process can be assumed. Since XPS spectra show an average of the entire area measured without information on the spatial distribution, the small amount of residual surface oxide is most likely a result of non-uniform mass transfer in static cells. In the static setup, i.e., without controlled convection, a lack of hydroxide leads to oxidation in some spots of the sample, particularly as the etch duration increases. For a concentration of 1 mM (Fig. 4b), SiO$_2$ was found on the surface of all samples. In contrast to elemental Si, the oxidation of SiC does not lead to the formation of an insulating SiO$_2$ layer. The SiO$_2$–SiC interface is reached after the first three sputter steps, i.e., a sputter depth of 11 nm. Silicon oxycarbide species are also present at the SiO$_2$–SiC interface. XPS measurements confirmed that for a concentration of 20 mM, SiC is etched, while in 1 mM KOH, a SiO$_2$ layer grows due to incomplete oxide dissolution. Since the dissolution of SiO$_2$ is extremely slow for such low concentrations and XPS measurements have proven an increase in layer thickness with time, a constant oxide growth must be assumed. In conclusion, the oxide layer does not add a large additional resistance to the reaction at this stage, which means it is not passivating the surface. This is only possible because the layer is non-insulating and (at least partially) permeable. At low potentials (e.g., 0 V), where the oxidation reaction is slow, such relatively thin oxide layers (approx. 12 nm after 5 min) do not yet impede the current flow. The same conclusion can be drawn from Fig. 5. With the increase in potential (data not shown), a significant increase in the SiO$_2$ layer was measured (37 nm). Hence, oxidation of SiC happens about three times faster at 0.5 V than at 0 V. For 1 V, the interface was not reached
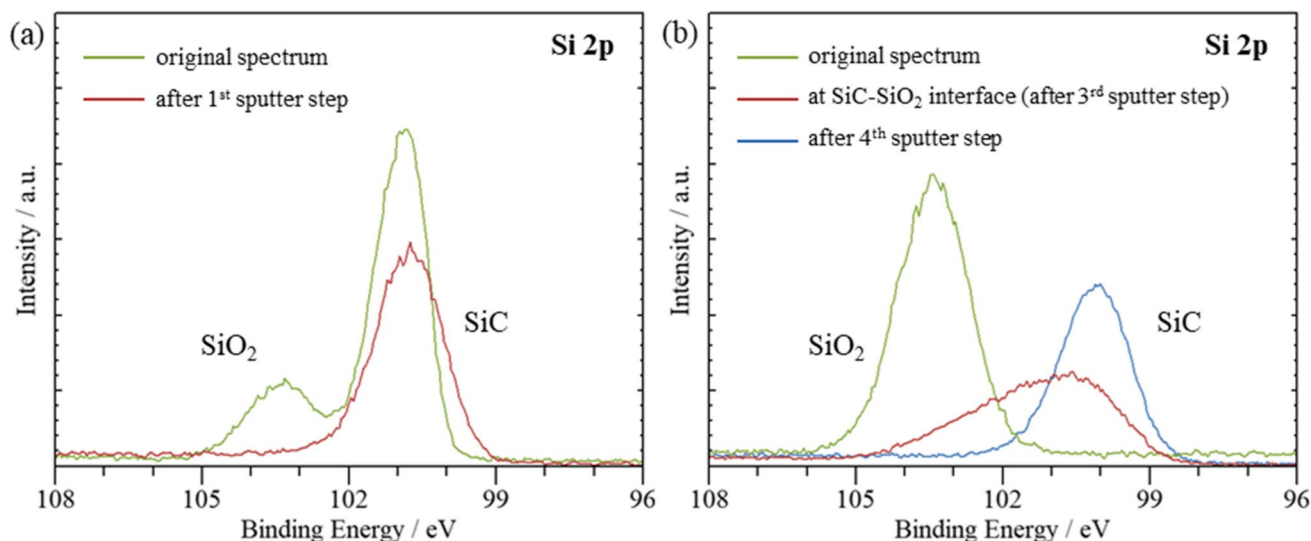
Fig. 4 Si(2p) spectra of the sample measured at 0 V in **a** 20 mM and **b** 1 mM KOH for 5 min before (initial spectrum) and after the first sputter step
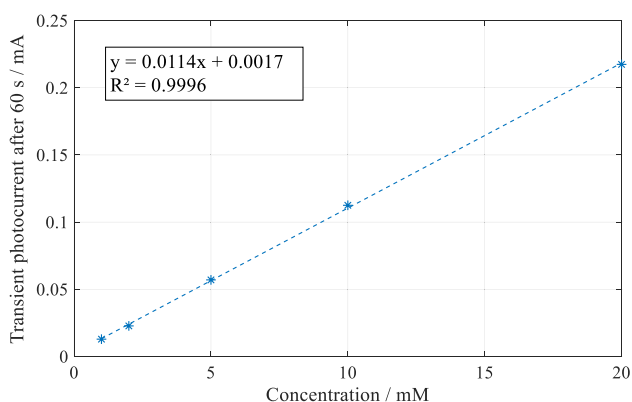
Fig. 5 Transient photocurrents after 60 s at 0 V as a function of electrolyte concentration

after the 7th step, indicating that the SiO_2 layer must be at least 6 times thicker than for 0 V. This implies that another mechanism must take over with increasing potentials. All XPS measurements performed in this work suggest only the formation of Si(IV) products, as no other oxidation states were found.

The potential of 0 V chosen for the transient measurements in Fig. 4 is still below $V_{i,max}$ for a concentration of 20 mM. For a concentration of 1 mM, however, the potential of 0 V lies in the range beyond the current peak, where oxide is formed. For 20 mM, a minimum in the current transient is observed before a constant etch rate is achieved. Such minima are commonly observed in crystallization or etching processes, as a certain over-potential is required to modify a pristine surface. In this case, the overpotential is probably needed to create the first etch sites. Afterward, the SiC is etched at a constant rate. This constant value represents the constant oxidation rate attained under steady-state conditions. The situation is different at 1 mM due to the growing SiO_2 layer on the surface. The residual constant current might be due to a constant growth in oxide thickness or an equilibrium of oxide formation and dissolution, which would lead to a constant layer thickness.

Figure 5 illustrates the transient photocurrent values taken from Fig. 3 after 60 s as a function of the hydroxide ion concentration. A perfectly straight line is obtained, i.e., there is a linear relationship between the steady-state current and the concentration, regardless of whether the oxide is completely dissolved (i.e., SiC is etched or oxidized, respectively). Hence, the oxidation reactions must continue independently of the dissolution reaction, resulting in oxide growth where the dissolution rate of SiO_2 is lower than the oxidation rate of SiC. Despite the formation of SiO_2 for low OH^- concentrations, the reaction rate at the given potential is directly proportional to the hydroxide concentration. This relationship indicates that at the given potential, the reaction rate (given through the photocurrent) is limited by the hydroxide concentration through mass transfer by diffusion. The relationship in Fig. 5 is only valid at sufficiently low potentials and short durations. At higher growth rates, more hydroxide ions are consumed. At the same time, their diffusion is impeded as the surficial oxide continues to grow thicker. The situation is different for higher potentials (e.g., 0.5 V), where the growth of the oxide layer happens much faster (data not shown), and the oxidation reaction with H_2O as an oxygen source contributes more noticeably to the overall current.

To obtain images of the surface, AFM measurements were performed for samples prepared at 0 V in 1 and 20 mM KOH solutions and compared to as-received samples. Since AFM is extremely sensitive to topographical changes, the time intervals for transient measurements were reduced to 5 to 120 s. RMS roughness values are enclosed in the insets. Figure 6b and c display two of these measurements for the sample oxidized in 1 mM at 0 V after 60 s and 120 s for two different scan sizes (1 μm × 1 μm and 5 μm × 5 μm). Parallelly oriented grooves originating from the sample preparation are visible on as-received samples. From XPS data, the surficial changes can be attributed to SiO_2 forming on the surface. The images show that after about 60 s, a thin (approx. 2 nm as calculated from the charge transferred during the reaction) and uniform SiO_2 layer has formed on the surface. The oxide layer is still somewhat porous and, therefore, permeable for the electrolyte. This explains why the oxide growth continues essentially unchanged. Compared to the untreated sample, there is only a slight increase in surface roughness. This is probably due to the slow growth rate. Also, the higher resistance of SiO_2 compared to the substrate leads to smoothing at the beginning of the oxide layer growth. Thus, oxide formation has a leveling effect. The grooves underneath the oxide layer are clearly recognizable after 60 s (Fig. 6b) and still visible after 120 s (Fig. 6c).

Almost no oxide is formed under the same conditions in 20 mM KOH (Fig. 4a), which is strong evidence that the material is dissolved. Figure 6d and e illustrate AFM measurements after two different durations of etching, i.e., 60, and 120 s. RMS values show more severe roughening of the surface than for the oxidation process. The change in surface morphology within these 5 min was not strong enough to be visible in SEM images. Measurement times had to be increased in order to observe the surface morphology of etched samples using SEM. Such an image after etching for 20 min is shown in Fig. 7. The image contains some lighter areas, indicating that some fraction of the surface was oxidized due to slow OH^- transport. After 20 min of polarizing the sample at 0 V in 20 mM KOH, etch pits are visible. Etch depths were determined using a profilometer after 10 min of etching. A maximum and an average value of about 299 nm and 209 nm were obtained, respectively. The calculated etch depth for this reaction is 294 nm for a reaction valence of $6 h^+$ (see Eq. (1)). However, precise calculations are difficult
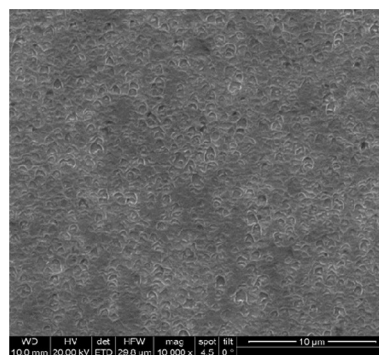
**Fig. 7** SEM images (top view) of samples treated in 20 mM KOH at 0 V for 20 min
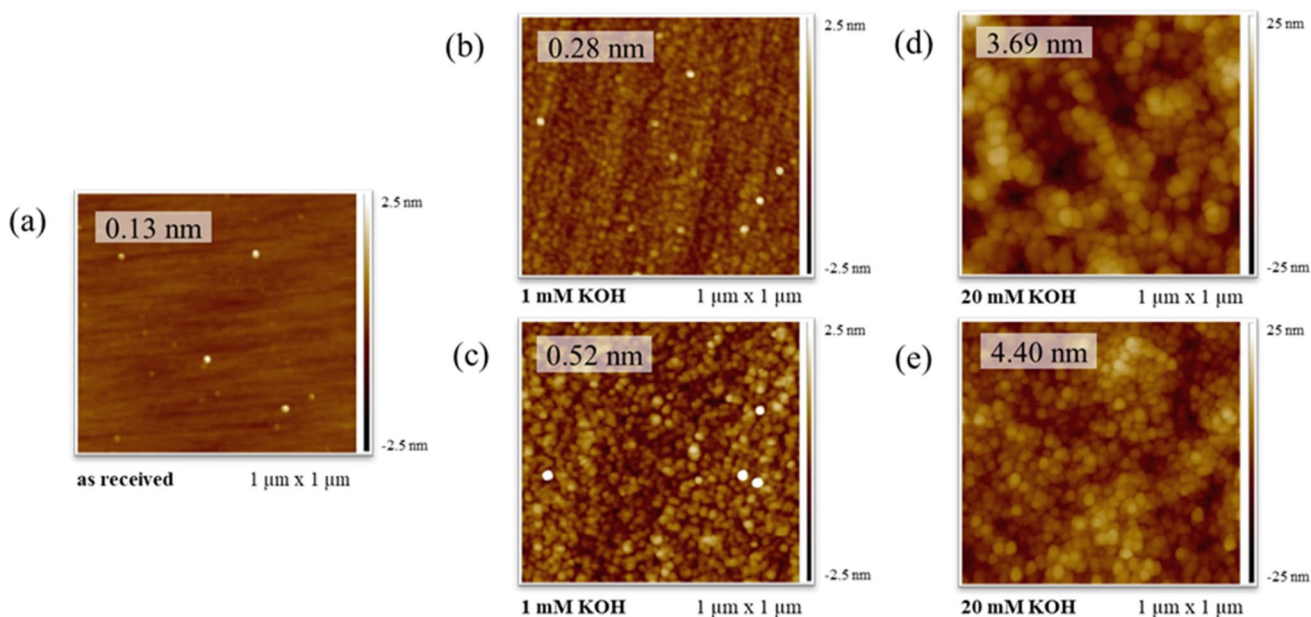
Fig. 6 AFM images for samples: as-received (**a**), treated at 0 V in 1 mM (**b**, **c**) and 20 mM (**d**, **e**) KOH for 60 s (**b**, **d**) and 120 s (**c**, **e**). RMS roughness values are enclosed in the insets

due to the uneven etching. The profile clearly shows some bumps and roughening.

The dissolution of SiC involves mass transfer, charge transfer, and the following chemical reactions as relevant electrode processes. Hydrodynamic methods help resolve the overlap of mass transfer and electron transfer as they enable the control of the diffusion conditions. In this way, a prevalent concentration dependence becomes more clearly visible. The IRDE cell design is most helpful in investigating low hydroxide ion concentrations, as hydrodynamic control will not contribute additional information in the case of limitation through electrode kinetics or photolimitation.

Dynamic measurements in the newly developed IRDE cell

Prior to experiments using rotation, static measurements were carried out in the IRDE setup at different light intensities (i_{LED}) and concentrations at a fixed potential of 0.5 V. The corresponding photoanodic currents (transient current measured after 10 s, after current becomes constant) vs. i_{LED} are depicted in Fig. 8. When the reaction is photolimited, i.e., for sufficiently high electrolyte concentrations and potentials, the photocurrent is directly proportional to the incident light intensity, which is governed by the forward current of the LED. This can be seen for the concentration of 20 mM, the photocurrent steadily increases with the forward current. The non-linearity stems from the non-linear relationship between i_{LED} and the radiant flux observed for this type of LED due to thermal effects, that lead to a non-linear relationship between the radiant flux and the forward current [30]. A similar trend is seen for lower concentrations for the first few points. However, the dashed line indicates a plateau
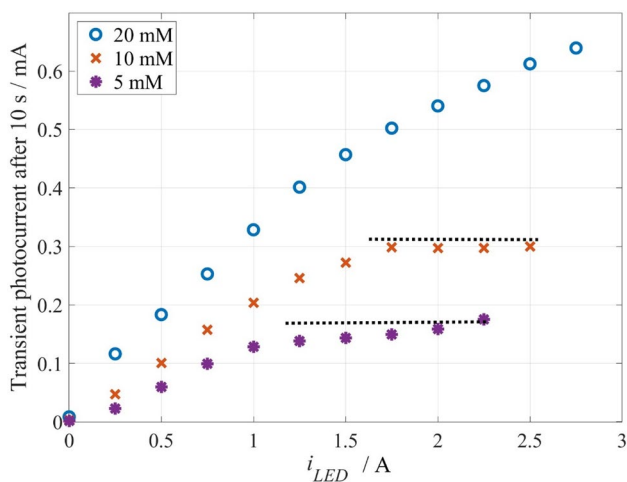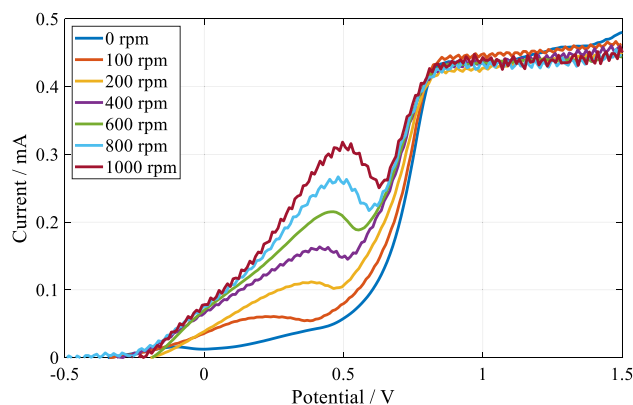
starting above 1.25 A and 1.75 A for 5 mM and 10 mM, respectively. In this region, the concentration is perspicuously dominant over the light intensity and, therefore, the most interesting for further investigation in the IRDE cell. These results coincide with what has been reported previously by Van Dorp et al. [18], where for low KOH concentrations (< 10 mM), a similar current plateau was observed when the light intensity was further increased. They concluded that in this range, the reaction was limited by the diffusion of hydroxide ions.

To further investigate the mass transport by diffusion of OH^-, cyclic voltammograms were performed in our newly developed IRDE cell [31]. The results are shown in Fig. 9 for rotation speeds from 0 to 1000 rpm. A concentration of 1 mM KOH was chosen to leave room for the rise in photocurrent expected from the increase in rotation speed. Smaller concentrations of the diffusing species are preferable for finding mass transport limitations, especially when working at a moderate light intensity ($i_{LED} = 1.5$ A). Two regimes are visible: (1) from − 0.2 to 0.7 V, the current depends on the rotation rate. (2) For potentials higher than 0.8 V, the rotation (i.e., the thickness of the diffusion layer) does not influence the current, indicating that this region is not under diffusion control. The current is instead limited by hole generation and dependent on the light intensity, as demonstrated in Fig. 8.

A higher rotation rate leads to a thinner Nernst diffusion layer (d_l), equivalent to an increase in concentration in OH^-. The the diffusion-limited current i_d under stationary conditions follows Eq. (10) [29].

$$i_d = z \cdot F \cdot D \cdot A \cdot (c_0 - c_S)/d_l \tag{10}$$

In Fig. 9, the peak potential $V_{i,max}$ shifts anodically with the rotation rate. Similar observations were made for the concentration dependence of the static CV measurements
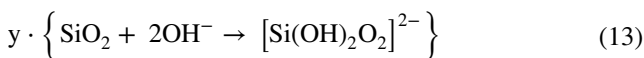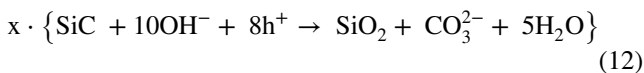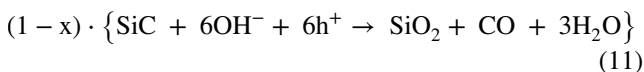

Fig. 8 Photoinduced anodic current measured for different concentrations of hydroxide ions as a function of LED driving current (light intensity) at a potential of 0.5 V after 10 s

Fig. 9 CVs measured in the IRDE at different rotation speeds in 1 mM KOH (+ 99 mM KNO$_3$) at a scan rate of 50 mV s^{-1}

in Fig. 1. The peak current i_{max} increases with the rotation rate, strongly suggesting diffusion control. This is in contrast to measurements by Van Dorp et al. who measured cyclic voltammograms in a conventional RDE cell at higher concentrations. Contrary to expectations, a decrease in the peak current with the increase in rotation rate was found in RDE measurements in 0.1 M solutions. In contrast, the shape of the current–potential plot remained basically unchanged. They concluded that improving the hydrodynamics may lead to faster passivation of the surface, which was linked to an enhanced interlinkage of silicate species with the removal of CO from surface sites [19]. As described previously, the concentration of the electrolyte solution is crucial for the mass transport. Thus, a real diffusion limitation might only become visible for such low concentrations as used in this work.

Similar to Fig. 1, the peak potential $V_{i,max}$ is shifted anodically with the rotation speed. As more hydroxide ions are available for the oxidation reaction, OH^- only becomes depleted at a higher current and, thus, potential. With an increase in rotation speed and a decrease in d_1 (equivalent to an increase in hydroxide ion concentration), the oxidation reaction goes on longer before OH^- becomes depleted.

To derive a quantitative relationship for the influence of hydroxide ions, two parameters, x and y, are introduced, where x is the fraction of CO_3^{2-} formed and y is the fraction of SiO_2 dissolved. For $x = 0$ and $x = 1$, CO and CO_2/CO_3^{2-} are exclusively formed as carbonous reaction products, respectively. A value of $y = 0$, therefore, is equal to the complete oxidation of SiC to solid SiO_2, whereas $y = 1$ represents a complete dissolution of SiC. The number of unit charges consumed in relation to the consumption of OH^- during the reaction is represented by z and ν is the stoichiometric number.

$$(1 - x) \cdot \left\{ SiC + 6OH^- + 6h^+ \rightarrow SiO_2 + CO + 3H_2O \right\} \tag{11}$$

$$x \cdot \left\{ SiC + 10OH^- + 8h^+ \rightarrow SiO_2 + CO_3^{2-} + 5H_2O \right\} \tag{12}$$

$$y \cdot \left\{ SiO_2 + 2OH^- \rightarrow [Si(OH)_2O_2]^{2-} \right\} \tag{13}$$

$$z = \nu_{h+}/\nu_{OH-} = (6 + 2x)/(6 + 4x + 2y) = (3 + x)/(3 + 2x + y) \tag{14}$$

The slope of the curve in the Levich plot is determined according to

$$i_{lim} = 0.62 \cdot z \cdot F \cdot c_0 \cdot A \cdot D^{2/3} \cdot \nu_{kin}^{-1/6} \cdot \omega^{1/2} \tag{15}$$

with an active surface area A of 0.25 cm^2, a bulk concentration c_0 of 10^{-6} mol cm^{-3}, the kinematic viscosity for water ($\nu_{kin} = 0.00992$ cm2 s^{-1}), and the diffusion coefficient for

OH^- ($D = 5.27 \times 10^{-5}$ cm^2 s^{-1}, [32]). It can be assumed that the diffusion coefficients of OH^- in free water (i.e., for infinite dilution) and 0.1 M KNO_3 are not significantly different since water molecules are determinative for the diffusion of both hydronium and hydroxide ions in aqueous solutions [33]. For comparison, the diffusion coefficient of OH^- is 5.8×10^{-5} cm^2 s^{-1} in 0.1 M KOH [34]. From Eq. (14), it can be seen that the maximum and minimum for z are $z_{max} = 1$ (for $x = 0$ and $y = 0$) and $z_{min} = 2/3$ (for $x = 1$ and $y = 1$), respectively. Lines for these two values for z are plotted in Fig. 10.

From the slope of the regression lines, the exact value of z is derived (0.87 and 0.78 for 400–1600 and 100–1000 rpm, respectively). However, the variance of these values caused by the experimental error is too large compared to the difference between the theoretical values to derive clear indications for the reaction mechanism. Still, Fig. 10 proves that the reaction is governed by the diffusion of hydroxide ions in this specific potential range.

Also, with the ongoing dissolution of the material, the concentration of available OH^- ions in the bulk solution decreases. Due to the uptake of OH^- ions during the reaction, a decrease in pH is expected. Typically, the difference in pH before and after the measurement was considerably larger than expected from the sheer use of OH^- in the reaction. A systematic determination of pH and conductivity values before and after each experiment could also help to calculate the amount of CO_2.

Simulation using an electrical network model

For sufficiently low scan rates, no peaks but limiting current plateaus are expected as the concentration at the boundary layer is held constant by means of controlled convection,
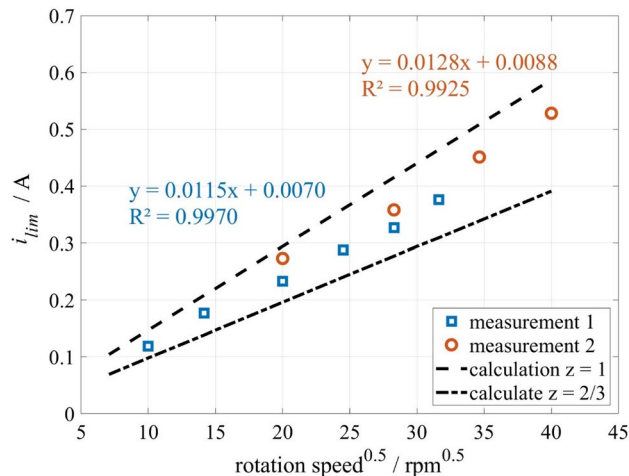

Fig. 10 Levich plots for two measurements in different rotation ranges. Calculated values are plotted for $z_{max} = 1$ and $z_{min} = 2/3$

i.e., the thickness of the diffusion layer does not expand over time. In contrast to voltammetric peaks, which are typically observed at higher scan rates or lower rotation rates, the peaks in Fig. 9 do not vanish at higher rotation rates but become more prominent. We hypothesize that the occurrence of the peak, as well as the dependence of the current maximum and minimum on the rotation rate, is due to the competing oxidation and dissolution processes or the change of the surface properties during the oxide formation. The relation between the oxidation rate of SiC and the dissolution rate of SiO_2 determines the peak current.

In this paper, we demonstrate that through meticulous selection of the reaction mechanism and potential-dependent reaction rates, it is possible to replicate the observed peak in a simulation. This clarification highlights that the peak is not a conventional voltammetric peak stemming from a dynamic process but rather can be attributed to stationary behavior. Nevertheless, it might coincide with the response associated with the transient formation of the diffusion layer. A more intricate understanding of the reaction mechanism is essential for elucidating the voltammogram shapes. The pertinent equations for the simulation are presented in Fig. 11.

For non-selective dissolution, where Si and C dissolve simultaneously, their dissolution rates are equal. Initially, the Faradaic reaction in Eq. (2) occurs, requiring oxygen from OH^- ions for oxide formation. As the OH^- concentration remains relatively high, SiO_2 dissolves as given by Eq. (3), resulting in Eq. (1) as the overall reaction at lower potentials. At more positive potentials, a limiting current emerges due to the diffusion-controlled mass transport of

hydroxyl ions across the Nernst diffusion layer, controlled by the IRDE. This constrains the overall oxidation rate. As the potential increases further, the reaction mechanism shifts. With fewer OH^- ions no longer available, water becomes the main oxygen source (see Eq. (4)). Since this reaction does not depend on hydroxyl ions, SiC oxidation is no longer diffusion-limited. However, the protons produced Eq. (5) consume hydroxyl ions, which are then unavailable for other reactions. Moreover, at high positive potentials, CO may further oxidize to CO_2 Eq. (6) or Eq. (7), consuming 2 additional OH^- ions and forming a carbonate.

The reaction was simulated using electrical network simulation due to the specialized nature of tools tailored for network simulation and their effectiveness in transient analysis. To achieve this, (electro-)chemical reactions were represented using electrical circuit elements, illustrated in Fig. 12. Specifically, a forward-connected diode model (D1) served as a substitute for the charge transfer reaction, with its parameters adjusted to mimic the exponential shape of the polarization characteristic observed in Faradaic reactions with charge transfer limitation. Similarly, a diode in reverse connection (D2) was employed to model stationary diffusion limitation, with the reverse current set to the required limiting current. The saturation current of the diode represents the limiting current of a diffusion-controlled electrochemical reaction. Thus, the change in saturation current stands for the different rotational speeds in the experiments. In the simulation circuit, "behavioral current sources" (BOH, BH2O) were employed to account for the effects of partial currents associated with the consumption of OH^- ions. The
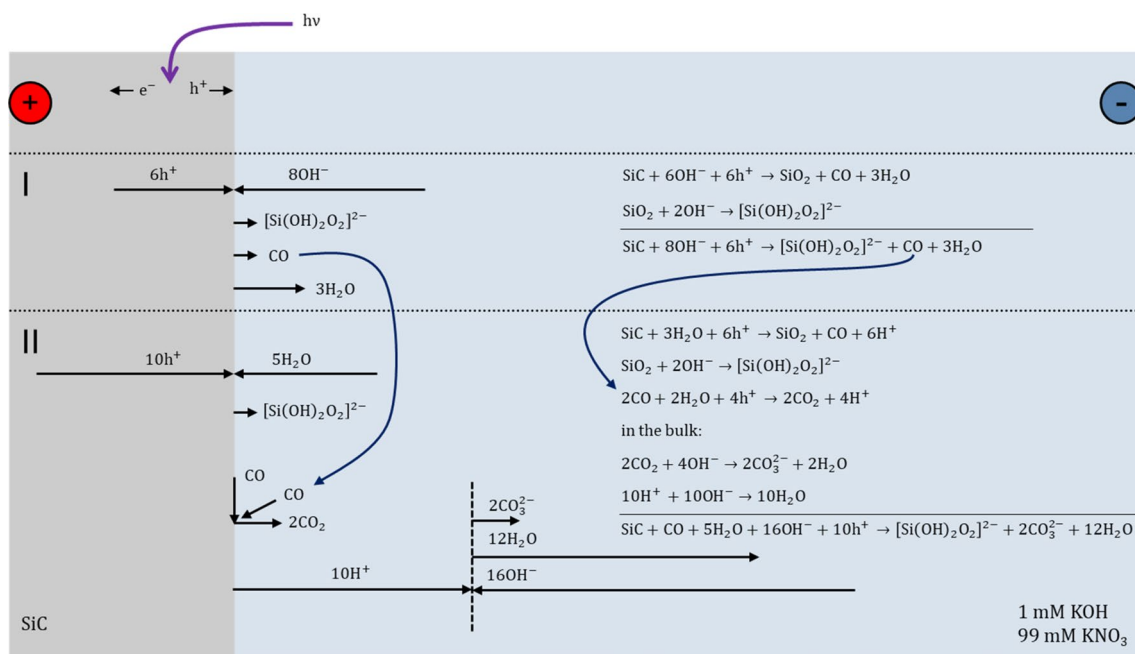

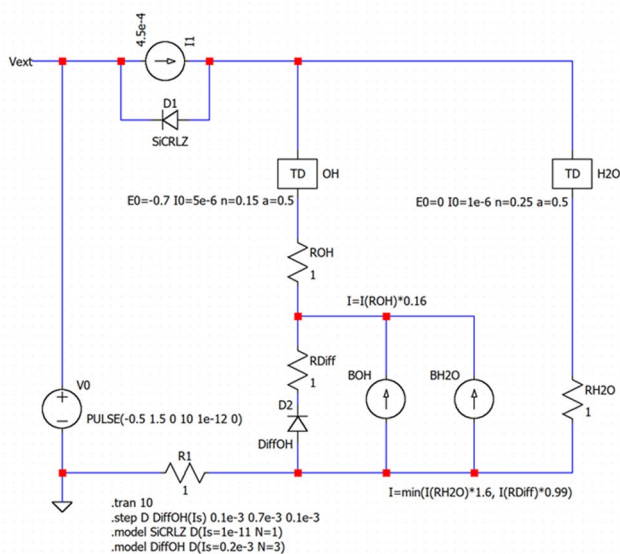**Fig. 11** Reaction model used as basis for network simulation

Fig. 12 LTspice © model used for network simulation

attributed to the potential dependence of variables x and y, as outlined in Eqs. (11–13).

Conclusion

The electrochemical behavior of 4H-SiC is strongly impacted by the formation of SiO_2 as a solid oxidation product. Etching and/or oxidation occur depending on the potential applied in relation to the reaction rates of SiC oxidation and SiO_2 dissolution. Particularly for electrolytes below a specific concentration, the dissolution rate of SiO_x products was too low, resulting in a surficial oxide layer. Changes in chemical composition ($SiC \rightarrow SiO_2$) were reliably detected using XPS, allowing to distinguish between different reaction regimes. AFM measurements illustrate the progress of surface oxidation and dissolution in the first minutes of the photoelectrochemical reaction and show the corresponding differences in surface roughness. At constant light intensity and electrode potential, the hydroxide ion concentration determines whether the material is oxidized or dissolved. This study leverages a novel electrochemical setup to investigate the influence of mass transfer on the photoassisted anodic reactions of silicon carbide (SiC). While similar studies exist in the literature, our redesigned cell offers distinct advantages, providing a more suitable platform for this specific type of reaction. Cyclic voltammograms in the IRDE cell at different rotation speeds allowed for a clear distinction between regimes limited by mass transfer (ion
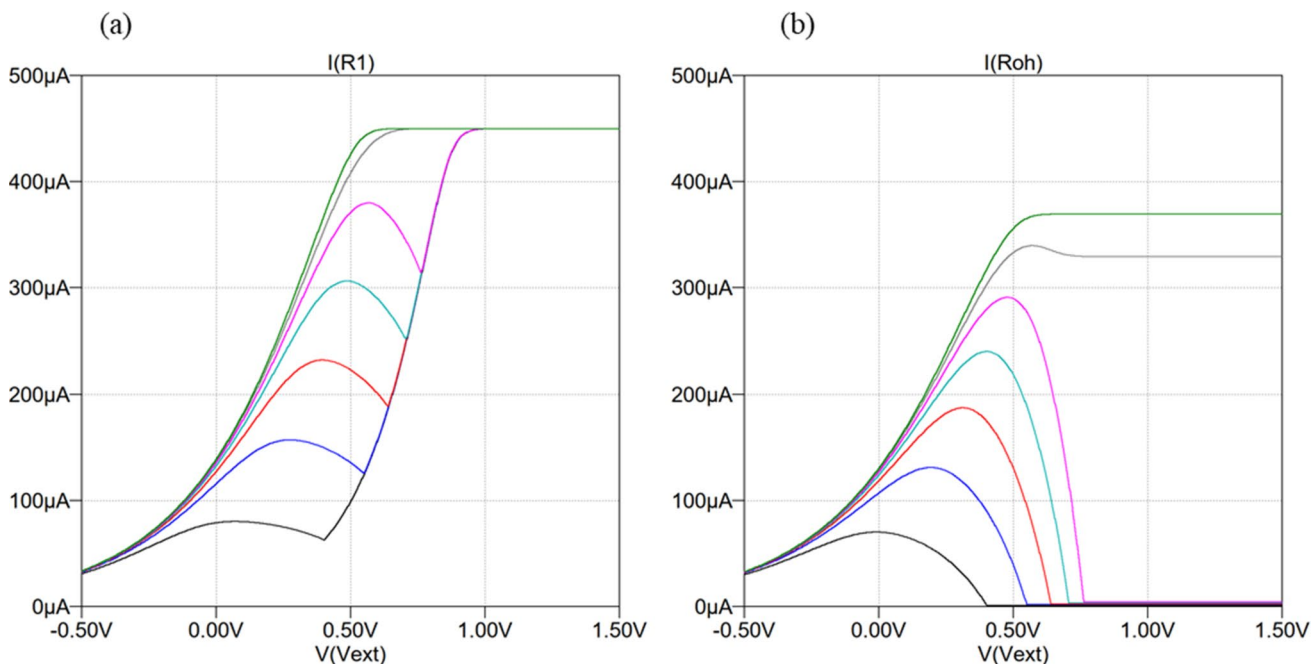
simulation results, depicted in Fig. 13, accurately captured the potential-dependent behavior of the diffusion-controlled current. Both the shift in peak potential and the peak current are distinctly observable. The peak maximum is clearly diffusion-dependent, reinforcing the experimental findings presented above. The residual deviation between simulated and experimental data, especially in the transition region between the peak and the photolimited current, is likely

Fig. 13 Simulation of **a** total current (IR1) and **b** currents for the partial reaction involving OH⁻ for different limiting currents (= saturation currents of D2) corresponding to different rotational speeds

concentration) and light intensity (hole concentration). The availability of OH⁻ ions determines the reaction rate at potentials below 0.75 V. The Levich plot analysis verified that the reaction in our specific potential range is governed by the diffusion of hydroxide ions and demonstrated information about the reaction mechanism. With this, it has been effectively confirmed that mass transport phenomena play a prominent role for KOH concentrations up to 0.02 M. Notably, our observations contrasted with previous studies, utilizing conventional RDE measurements, emphasizing the importance of a reliable electrochemical setup and the influence of the experimental parameters. Utilizing a network model grounded in a comprehensive reaction mechanism, our study substantiated both the diffusion-controlled dynamics and the distinct electrochemical behavior arising from competing reactions. In summary, our work not only contributes to advancing the understanding of photoassisted anodic reactions on silicon carbide but also underscores the critical role of experimental setup design in unraveling complex electrochemical processes.

Materials and methods

Electrochemical measurements

Silicon carbide wafers were supplied in the form of square-cut pieces of 10 mm × 10 mm with a proprietary backside metallization providing an Ohmic contact. The material has a nominal doping level of 8×10^{15} cm^{-3}, and its resistivity ranges from 0.012 to 0.025 Ω cm. All experiments were performed on the Si face (0001), with substrates being 4° off-axis. When smaller pieces were required, samples were cleaved into quarters with a diamond scriber. Procedures for sample preparation varied depending on the electrochemical setup utilized. In any case, a wire (copper or platinum) was soldered onto the backside of the wafer for electrical contact. For measurements performed in the IRDE, embedding was required to avoid contact between metals (i.e., backside metallization, solder, and wire) and electrolyte solution. ProntoFix® resin and a ProntoFix® hardener from Struers were mixed in a ratio of 3.6:1 for embedding samples into cylindrical resin bodies with a diameter of 15 mm and a height of 10 mm. Embedded samples used in IRDE experiments were additionally provided with a thin gold layer on the backside to increase electric contact. Sputter deposition was done using an Ar⁺ sputter device. Only square samples were available. To improve the current density distribution on the surface of the semiconductor, samples were quartered (5 mm × 5 mm) for experiments in the IRDE. All samples (with or without embedding) were cleaned using ethanol and deionized water before each experiment.

Chemicals used for the preparation of electrolytes include solid potassium hydroxide (KOH, Merck, per analysis) and potassium nitrate (KNO₃, ≥ 99.0%, crystals, BAKER ANALYZED® ACS, J.T. Baker®). A potentiostat/galvanostat Autolab PGSTAT204 by Metrohm operated with Nova 2.1 was used for all electrochemical measurements. All potentials reported in this study were measured versus an Ag|AgCl|1 M KCl reference electrode unless otherwise mentioned. Either a platinum sheet or a platinum wire was used as a counter electrode. For cyclic voltammograms, both the scan rate and the number of scans directly influence the duration of an experiment. Experiments were kept as short as possible to prolong the lifetime of the UV-LED light source and electronic components, avoid thermal effects, and preserve constant experimental conditions. Typically, only 1–3 scans are performed with a scan rate of 50 mV s^{-1}. Aqueous solutions of KOH with concentrations ranging from 0.1 to 50 mM were prepared. KNO₃ was added to each of these solutions as a supporting electrolyte to decrease the solution resistance. Furthermore, the supporting electrolyte minimizes the number of reactant ions involved in the migration process.

Two different concepts for experimental setups are described for this study. A static electrode cell allowed for the preparation of samples for surface analysis in a wide range of electrochemical process parameters. This sample holder does not require the sample to be embedded. The electrolyte reservoir with an inner diameter of 30 mm holds a liquid volume of about 3–6 cm³. A platinum wire placed at the inner sidewall leads outside through a small side opening and is used as the counter electrode. The reference electrode is placed in a separate liquid reservoir. A hose filled with electrolyte solution connects the two liquid reservoirs to provide ionic contact. Leak tightness is provided by pressing a backplate and the sample against the inner opening of the holder. Only a circular section with a diameter of 4 mm is exposed to the electrolyte and illumination in this setup.

A new inverted rotating disk electrode setup was designed, optimized and validated for the purpose of this work, as depicted in Fig. 14. This new inverted setup based on magnetic coupling facilitates the homogenous illumination of the electrode surface and allows for the removal of gaseous reaction products [31].

A high-power LED with a nominal wavelength of 365 nm and an output power of 10.6 W (LUMINUS SBM-120-UV [30]) was used as a light source. The irradiance on the sample was determined using a photodiode (S1223-01 by Hamamatsu [35]). Unless otherwise mentioned, the light intensity was kept constant by setting the forward current through the LED (i_{LED}) to 1.5 A and adjusting the distance between the sample and the light source (d_{LED}) to 20 mm. For these operational parameters, the irradiance E_e was determined to be ~ 0.95 W cm^{-2}.
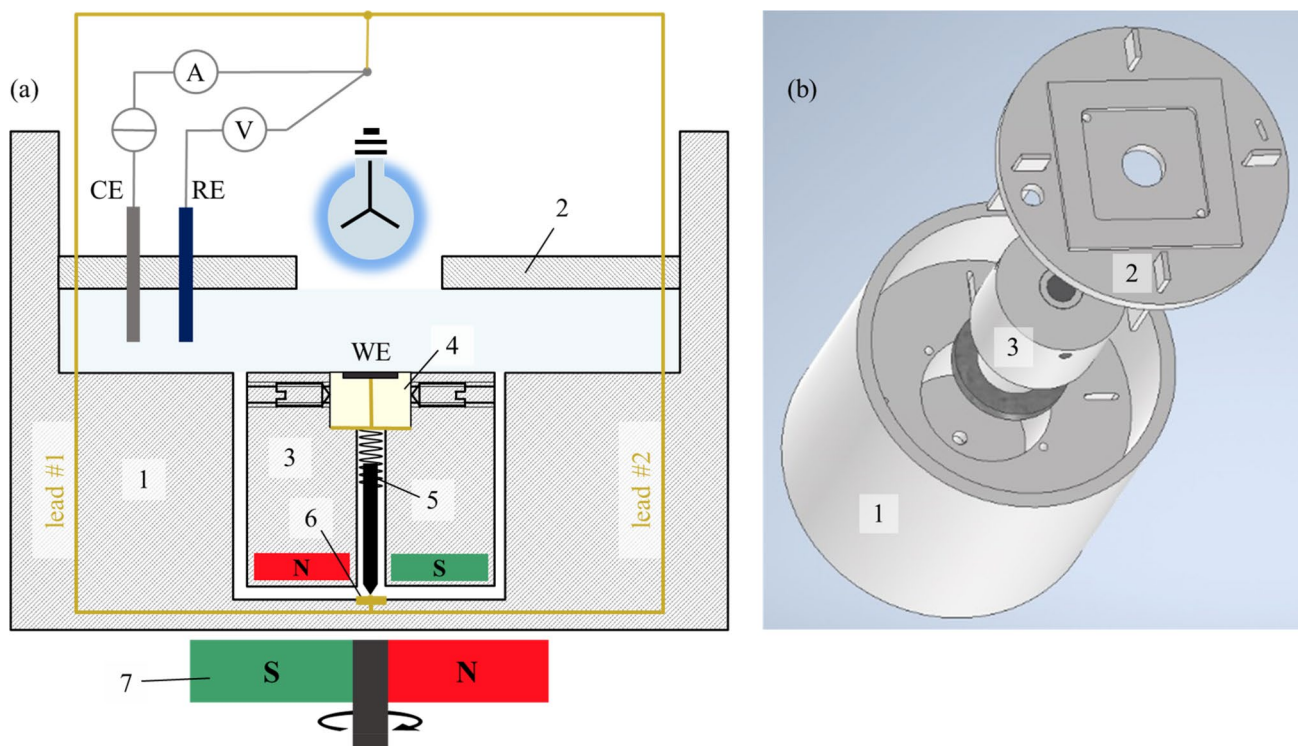
1   static electrolyte reservoir
2   cover with feedthrough for counter electrode, reference electrode and window for illumination
3   rotor with locking plastic headless screws and follower ring magnet
4   epoxy resin cylinder with working electrode and gold contact on the backside
5   Pt/Ir spring loaded graphite rod
6   gold contact plate with lead #1 and lead #2
7   driver magnet

Fig. 14 **a** Schematic sketch and **b** CAD construction of the newly developed IRDE cell. Reproduced from [31] with permission from Elsevier

Analytical measurements

SEM–EDX was carried out using SEM FEI Quanta 200 with accelerating voltages between 5 and 20 kV. Tapping-mode AFM was performed using a Nanoscope VIII (Bruker) under ambient conditions on sampling sizes from 1 μm × 1 μm to 10 μm × 10 μm. The scan rate was 4 Hz. On a larger depth scale (> 200 nm), etch profiles were measured using a profilometer DektakXT (Bruker).

The μFocus 350 XPS system (by Specs) uses a monochromatic $Al_{K\alpha}$ X-ray source that operates at an excitation energy of 1486.6 eV, an emission current of 7 mA, and an output energy of 100 W. The UHV system works at a pressure of 10^{-9} mbar. Software by Specs and CasaXPS was used for data evaluation. Typically, adventitious carbon is used as a reference signal with the C−C bonds relating to a binding energy of 284.8 eV. For SiC samples, the carbon signal is not characteristic of adventitious carbon but rather the C atoms within the SiC crystal (with a binding energy of about 283 eV). Compared to Si−C, C−C bonds show a low intensity, sometimes making them ineligible as a reference. Also, when surface impurities are removed by sputtering, the adventitious carbon signal is no longer available for correcting the spectra. If surfaces rich in oxygen (such as SiO_2) are characterized, another possibility is to fixate the binding energy for O(1 s) in a way that the C(1 s) peak (or shoulder) falls on the correct value [36]. In these cases, the O(1 s) peak with 532.2 eV was used as a reference, corresponding to a C(1 s) peak of 284.8 eV. A Gaussian function with 20% Laurentian was used for peak fitting. Background fits were done either with a U2Tougaard (SiO_2 present) or a Shirley background (no SiO_2 present). Reference spectra for both pure SiC and SiO_2 samples were measured. For depth profiles, sputter and analysis steps were alternated several times. Ar^+ sputtering was performed using

a sputter device (IQE 12/38) at a pressure of 2.00×10^{-7} mbar and a voltage of 3 kV. For the SiO_2 reference, a sputter profile was done to determine the sputter rate, which was 2 nm min^{-1}.

Data availability Not applicable

References

1. Langpoklakpam C, Liu AC, Chu KH, Hsu LH, Lee WC, Chen SC, Sun CW, Shih MH, Lee KY, Kuo HC (2022) Crystals 12:245
2. Östling M, Ghandi R, Zetterling CM (2011) SiC power devices—present status, applications and future perspective. In: 2011 IEEE 23rd international symposium on power semiconductor devices and ICs, p 10. San Diego, CA, USA
3. She X, Huang AQ, Lucia O, Ozpineci B (2017) IEEE Trans Ind Electron 64:8193
4. Jiang L, Cheung R (2009) Int J Comput Mater Sci Surf Eng 2:227
5. Wright NG, Horsfall AB (2007) J Phys D: Appl Phys 40:6345
6. Oliveros A, Guiseppi-Elie A, Saddow SE (2013) Biomed Microdevices 15:353
7. Kimoto T, Cooper J (2014) Fundamentals of silicon carbide technology: growth, characterization, devices and applications. John Wiley & Sons, Singapore, p 2
8. Han L, Liang L, Kang Y, Qiu Y (2021) IEEE Trans Power Electron 36:2080
9. Lukin DM, Dory C, Guidry MA, Yang KY, Mishra SD, Trivedi R, Radulaski M, Sun S, Vercruysse DS, Ahn GH, Vučković J (2020) Nat Photonics 14:330
10. Shor JS, Kurtz AD (1994) J Electrochem Soc 141:778
11. Maboudian R, Carraro C, Senesky DG, Roper CS (2013) J Vac Sci Technol A 31:050805
12. Zhuang D, Edgar JH (2005) Mater Sci Eng R 48:1
13. Morisaki H, Ono H, Yazawa K (1984) J Electrochem Soc 131:2081
14. Shor JS, Zhang XG, Osgood RM (1992) J Electrochem Soc 139:1213
15. Shor JS, Osgood RM (1993) J Electrochem Soc 140:L123
16. Shor JS, Grimberg I, Weiss BZ, Kurtz AD (1993) Appl Phys Lett 62:2836
17. Kato M, Ichimura M, Arai E, Ramasamy P (2003) Jpn J Appl Phys 42:4233
18. Van Dorp DH, Weyher JL, Kelly JJ (2007) J Micromech Microeng 17:S50
19. Van Dorp DH, Kelly JJ (2007) J Electroanal Chem 599:260
20. Van Dorp DH, Sattler JJHB, Den Otter JH, Kelly JJ (2009) Electrochim Acta 54:6269
21. Van Dorp DH, Kooij ES, Arnoldbik WM, Kelly JJ (2009) Chem Mater 21:3297
22. Zhao F, Islam MM, Huang CF (2011) Mater Lett 65:409
23. Leitgeb M, Zellner C, Schneider M, Schmid U (2016) ECS J Solid State Sci Technol 5:P556
24. Leitgeb M, Zellner C, Hufnagl C, Schneider M, Schwab S, Hutter H, Schmid U (2017) J Electrochem Soc 164:E337
25. Whiteley S, Sorensen A, Vajo JJ, Sfadia R, Ladd TD, Cui S, Graetz J (2023) J Electrochem Soc 170:036508
26. Memming R (2001) Semiconductor electrochemistry. Wiley-VCH, Weinheim, p 260
27. Lauermann I, Memming R, Meissner D (1997) J Electrochem Soc 144:73
28. Shishkin Y, Choyke WJ, Devaty RP (2004) J Appl Phys 96:2311
29. Bard AJ, Faulkner LR (2001) Electrochemical methods: fundamentals and applications. John Wiley & Sons, Hoboken (NJ), p 163 & 340
30. LUMINUS (Online) https://www.luminus.com/products/uv. Accessed 31 Dec 2024
31. Mairhofer K, Rosenauer P, Nelhiebel M, Radl S, Larisegger S, Fafilek G (2022) J Electroanal Chem 917:116392
32. Haynes WM (2014) Handbook of chemistry and physics. CRC Press, Boca Raton, FL, p 5
33. Tuckerman ME, Marx D, Parrinello M (2002) Nature 417:925
34. Drexler CI, Miller TC, Rogers BA, Li YC, Daly CA, Yang T, Corcelli SA, Cremer PS (2019) J Am Chem Soc 141:6930
35. HAMAMATSU (Online) https://www.hamamatsu.com/eu/en/product/optical-sensors/photodiodes/si-photodiodes/S1223-01.html. Accessed 31 Jan 2024
36. Önneby C, Pantano CG (1997) J Vac Sci Technol A 15:1597

Publisher's Note Springer Nature remains neutral with regard to jurisdictional claims in published maps and institutional affiliations.

Authors and Affiliations

Katharina Mairhofer[1] · Silvia Larisegger[2] · Annette Foelske[3] · Markus Sauer[3] · Gernot Friedbacher[1] · Günter Fafilek[1]

✉ Günter Fafilek
guenter.fafilek@tuwien.ac.at

1. Technische Universität Wien, Getreidemarkt 9, 1060 Vienna, Austria

2. Kompetenzzentrum Automobil- und Industrieelektronik GmbH, Villach, Austria

3. Analytical Instrumentation Center, Technische Universität Wien, Lehargasse 6, 1060 Vienna, Austria